Strong, machinable and insulating chitosan-urea aerogels: towards ambient pressure drying of biopolymer aerogel monoliths

Natalia Guerrero Alburquerque[1,2], Shanyu Zhao[1]*, Nour Adilien[1], Matthias M. Koebel[1], Marco Lattuada[2], Wim J. Malfait[1]*

[1] *Laboratory for Building Energy Materials and Components, Swiss Federal Laboratories for Materials Science and Technology, Empa, Überlandstrasse 129, CH-8600 Dübendorf, Switzerland*

[2] *Department of Chemistry, University of Fribourg, Chemin du Musée 9, CH-1700 Fribourg, Switzerland*

Abstract - Biopolymer aerogels are an emerging class of materials with potential applications in drug delivery, thermal insulation, separation and filtration. Chitosan is of particular interest as a sustainable, biocompatible and abundant raw material. Here, we present urea-modified chitosan aerogels with high surface area and excellent thermal and mechanical properties. The irreversible gelation of an acidic chitosan solution is triggered by the thermal decomposition of urea at 80°C through an increase in pH and, more importantly, the formation of abundant ureido terminal groups. The hydrogels are dried using either supercritical (SCD) or ambient pressure (APD) methods to elucidate the influence of the drying process on the final aerogel properties. The hydrogels are exchanged into ethanol prior to SCD, and into ethanol and then heptane prior to APD. The surface chemistry and microstructure are monitored by solid-state NMR and FTIR spectroscopy, SEM, and nitrogen sorption. Surprisingly, large monolithic aerogel plates (70 mm^2) can be produced by APD, albeit at a somewhat higher density (0.17-0.42 g/cm^3). As prepared aerogels have thermal conductivities of ~24 and ~31 mW/(m·K), and surface areas of 160-170 and 85-230 m^2/g, for SCD and APD, respectively. For a primarily biopolymer-based material, these aerogels are exceptionally stable at elevated temperature (TGA) and char and self-extinguish after direct flame exposure. The urea-modified chitosan aerogels display superior mechanical properties compared to traditional silica aerogels, with no brittle rupture up to at least 80% strain, and depending on chitosan concentration, relatively high *E*-moduli (1.0-11.6 MPa) and stress at 80% strain values (σ_{80} of 3.5-17.9 MPa). Remarkably, the aerogel monoliths can be shaped and machined with standard tools, e.g. drilling and sawing. This first demonstration to produce monolithic and machinable, mesoporous aerogels from bio-sourced, renewable, non-toxic precursors, combined with the potential for reduced production cost by means of simple APD, opens up new opportunities for biopolymer aerogel applications and marks an important step towards commercialization of biopolymer aerogels.

Keywords: Mesoporous materials; Aerogel; Xerogel; Chitosan; Ureido; Ureylene; Urea

* wim.malfait@empa.ch, +41 58 765 4983; shanyu.zhao@empa.ch, +41 58 765 4244

1. Introduction

Aerogels are highly porous, predominantly mesoporous solids with exceptional properties and a rapidly growing market, particularly for silica aerogel as thermal superinsulation [1–4]. Traditionally, aerogels are prepared by extracting a gel's pore fluid with supercritical CO_2 drying (SCD) to circumvent the strong capillary forces that occur at liquid-gas interfaces during solvent evaporation. Supercritical drying however is a high pressure process that requires nontrivial equipment and is limited in terms of its economy of scale potential. Ambient pressure drying (APD) is a viable alternative to produce high quality silica aerogels if the gel surfaces have been hydrophobized [5], but is generally not feasible for hydrophilic aerogel systems because of excessive shrinkage and structural collapse.

Biopolymer aerogels are a potentially more sustainable alternative to silica aerogel, and a wide variety of precursors are available, mostly polysaccharides (e.g. cellulose, alginate, chitin and chitosan, pectin, starch), but also proteins and lignin [6]. Chitin and its deacetylated product chitosan are of particular interest because they are derived from shrimp and crab shell waste, of which six to eight million tonnes are produced per annum [7,8]. In addition, chitosan's amino groups, from the (deacetylated) d-glucosamine units, can impart its corresponding aerogels with specific functionality, including CO_2 sorption [9,10], metal ion absorption [9,11,12], dye absorption [13,14], trapping of contaminants[15,16], catalysis [17–23], reinforcement of other (e.g. silica) aerogels [24], chitosan derivatives [25–27], use as an encapsulation matrix for small molecules and nanoparticles [25,28–30], in addition to the traditional thermal insulation application [13,31–33].

The gelation of chitosan solutions can be induced either by means of i) physical mechanisms, e.g. by a pH or temperature change, ii) by coagulation in non-solvents, or iii) through (covalent) cross-linking with reactive cross-linkers. A first physical gelation mechanism uses pH, sometimes combined with temperature, to induce gelation. Dripping an acidic aqueous solution of chitosan into an alkaline solution causes coagulation due the pH inversion effect [34,35] and also a pH lowering gelation through pressurized CO_2 induces chitosan gelation [36], but the gelation is reversible and chitosan can be dissolved again upon acidification [37,38]. Physical gelation can also be induced by raising the temperature of a chitosan solution, buffered to a neutral pH by β-glycerolphosphate [39]. Increased temperatures were also used to cross-link hemicellulose citrate with chitosan at low pH [40]. Another physical gelation strategy involves coagulation of chitosan in a non-solvent [41] in a process akin to that for the production of regenerated cellulose aerogels [42]. Immersion in ethanol facilitated the gelation of polysaccharide aerogels without further addition of cross-linkers, but the resulting aerogels had limited mechanical strength [43]. Even for cross-linked chitosan gels, solvent-chitosan interactions, including the solvent exchange into CO_2 during supercritical drying, strongly affect the microstructure and properties [44].

Although chitosan is a non-toxic, renewable precursor, gels and aerogels are often produced by cross-linking the amino groups with "non-friendly" and often toxic cross-linkers, particularly formaldehyde [13,15,31,32,45], glutaraldehyde [15,16,46], glyoxal [15], and diisocyanates [27], which negates some of the benefits of using a sustainable, bio-sourced precursor. However, there are effective techniques to eliminate the

remains of these cross-linkers, for example the removal of glutaraldehyde using a mixture of CO_2 and ethanol during supercritical drying [47]. In addition, more benign cross-linkers are available, but have been applied only sporadically to the synthesis of chitosan aerogels. Cross-linking amino groups with CO_2 has not yet been applied to chitosan, but has been demonstrated successfully to produce polyurea from synthetic polyamines, either in pressurized reactors [48], or by bubbling CO_2 through a polyallylamine solution [49]. Urea is a possible cross-linker for amino groups that has been mostly overlooked in the latest non-isocyanate polyurea-polyurethane and aerogel literature. Before the advent of isocyanates, urea was the preferred cross-linker for polycondensation of polyurea, with a rich patent literature going back as far as the 1930s [50–52]. Typically large diamines or alkanolamines were reacted with urea in bulk or in solution at relatively high temperature (~200 °C) through the reaction:

$$2 \text{ R-NH}_2 + \text{H}_2\text{NCONH}_2 \longrightarrow \text{R-NHCONH-R} + 2\text{NH}_3$$

A recent study describes the urea-chitosan combination to produce gels [53], working with urease to accelerate the hydrolysis of urea [54]. Very recently, Ganesan et al. demonstrated a facile method to synthesize ureido-modified chitosan gels and aerogels [55].

In this study, we investigate the preparation of chitosan aerogels with high surface area and mesoporosity, and excellent mechanical and thermal properties using a urea modification. Both supercritical and, surprisingly, ambient pressure drying can yield large, defect-free monolithic aerogel plates. The gelation mechanism is probed using FTIR and solid-state NMR spectroscopic data which – in combination with complimentary characterization techniques - allows us to systematically map out the effect of chitosan concentration and drying conditions on shrinkage, density, microstructure, thermal conductivity and mechanical properties.

2. Experimental

2.1 Materials

Chitosan from crab shells with high viscosity (> 400 mPa.s for 1% in acetic acid @20°C), high molecular weight (HW) (310000-375000 g mol $^{-1}$) and a degree of deacetylation (DDA) of 77 %, urea BioXtra, a 320 g mol^{-1} cetyltrimethylammonium chloride (CTAC) solution, and HCl ACS Reagent (HCl 37 %) were purchased from Sigma Aldrich (Switzerland). Ethanol (F25-AF-MEK ethanol denatured with 2 % methyl ethyl ketone) was sourced from Alcosuisse, Switzerland. Heptane (isomer mixture, UN 1206) was obtained from Brenntag (Switzerland). Deionized water was used for dilutions. All reagents and solvents were used as received without further purification.

2.2 Synthesis of chitosan-urea aerogels

Let us explain the aerogel synthesis by example of a typical sample prepared from 10 % m/v chitosan solution (Fig. 1); preparations for other concentrations are summarized in Table S1. Aerogels were prepared by dissolving 4 g chitosan in 40 mL of a 1.12 M HCl aqueous solution under constant stirring at 70 °C in an oil bath for approximately 2 hours. The resulting, somewhat viscous, yellowish–transparent solution was taken out of the oil-bath and left to cool at room temperature for 5 minutes under stirring. After the dissolution of 9 g of urea, a very minor amount of surfactant (30 µL CTAC) was added to help eliminate bubbles. The solution was then centrifuged at 6000 rpm for 3 minutes to eliminate residual trapped air and possible insoluble solids which were removed by decantation. The chitosan-urea solution was poured into square silicone molds (25 ml of sol in 5x5x3 cm^3 for SCD, 60 ml of sol in 9x9x3 cm^3 for APD) and placed into a larger plastic polypropylene sample storage container. Gelation and aging took place at 80 °C for 24 h. Over the course of the gelation and aging process, the pH value changed from ~0 to 7.
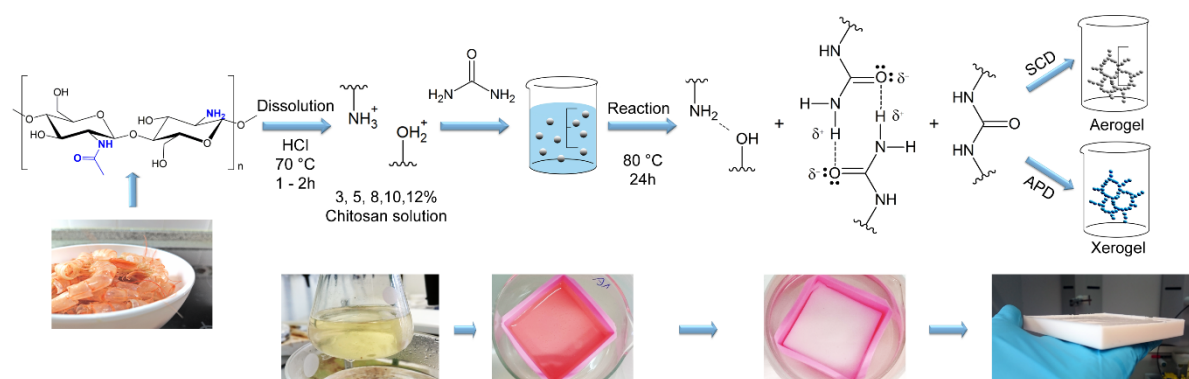

Figure 1. Chitosan aerogel synthesis and gelation mechanism.

The gels intended for SCD were exchanged into ethanol 3 times (gel:solvent ratio 1:10, 65 °C, 24 h each) and then dried from supercritical CO_2 (SCD) in an autoclave (4334/A21-1 Separex, France). The ethanol pore fluid was exchanged into liquid CO_2 at ~7 °C in a batch type autoclave. After several flushing steps with liquid CO_2 during ~8h, the ethanol was exchanged with CO_2. The chamber was isolated from the CO_2 supply and the temperature was increased to 50 °C over the course of about 4 h, leading to an increase in pressure of typically 150 bar. Subsequently, the supercritical CO_2 autoclave was depressurized within 1 h and allowed to cool to room temperature prior to removing the samples. A second set of samples was prepared by ambient pressure drying. Here, as prepared gels were washed thrice with ethanol (gel: solvent ratio 1:10, 65 °C, 24 h per washing step), and then exchanged into heptane 3 times (gel: solvent ratio 1:10, 25 °C, 24 h per exchange step). The samples were then allowed to dry at ambient pressure in open containers, either at room temperature or at 65 °C.

2.3 Characterization

The linear shrinkage of the gels for each of the processing steps was monitored by measuring the edge length of the square samples with a caliper, $(L-L_0)/L_0$, where L is the length of the sample after each

processing step and L_0 is the length of the sample container. The size of the relatively weak hydrogels could not be determined accurately, but the shrinkage after gelation and aging was minimal (between 0 and 2%) for all hydrogels. The apparent bulk density was calculated from the weight and the dimensions of the regularly shaped monolithic samples (square plates, cylinders). The skeletal density ($\rho_{skeletal}$) was measured by helium pycnometry (AccuPyc II 1340). No degassing was performed prior to the density measurements. The pore volume (V_{pore}) along with the porosity (%ϕ) was calculated from the bulk and skeletal density of the aerogel [Eq.1-2].

$$V_{pore} = \frac{1}{\rho_{bulk}} - \frac{1}{\rho_{skeletal}} \qquad \text{Eq.1}$$

$$\% \, \phi = \left(1 - \frac{\rho_{bulk}}{\rho_{skeletal}}\right) \cdot 100 \quad \text{Eq.2}$$

Nitrogen sorption isotherms were measured at liquid nitrogen temperature on a Micromeritics TriFlex instrument after degassing the samples at 3.3×10^{-2} mbar and 80 °C for 40 h. The specific surface areas (S_{BET}) were calculated from 4-6 data points in the linear range of P/P_0 between 0.05 and 0.3 using the BET (Brunauer-Emmett-Teller) method. The S_{BET} and C-values are listed in Table 1 and Table S10. The average pore diameter was calculated from the pore volume and surface area assuming cylindrical pores [Eq.3], rather than the classical BJH (Barrett-Joyner-Halenda) model for analysis [56], which for aerogel is affected by mechanical deformation in the desorption branch of the capillary condensation range [57]. The precision of the BET surface area is approximately 10 m^2/g, but the accuracy may be lower (around 50 m^2/g) because of model dependencies.

$$D_{pore} = \frac{4 \cdot V_{pore}}{S_{BET}} \qquad \text{Eq.3}$$

Scanning electron microscopy (SEM) images were recorded with an FEI Nova NanoSEM 230 (FEI, Hillsboro, Oregon, USA) at an accelerating voltage between 5 and 10 kV and a working distance around 5 mm. The samples were fixed using carbon pads and coated with Pt at a nominal thickness of 20 nm. Note that the actual thickness of the coating on the aerogel surfaces is much lower because of the extreme topography.

Solid-state NMR spectra were acquired with a Bruker Avance III system equipped with a wide-bore 9.4 T magnet, corresponding to Larmor frequencies of 400.2 MHz for ^{1}H and 100.6 MHz for ^{13}C, using 7 mm diameter zirconia rotors and a magic angle spinning (MAS) rate of 4 kHz. ^{1}H-^{13}C cross polarization spectra were acquired using a recycle delay of 3 s and a relatively long contact time of 2 ms to minimize the dependency of the relative spectral intensities on the hydrogen-carbon distance. Fourier Transform Infrared (FTIR) spectra were collected with a Bruker Tensor 27 FTIR spectrophotometer with a scan range from 400 to 4000 cm^{-1}. Spectra were collected in Attenuated Total Reflectance mode (ATR) using a diamond crystal.

The thermal conductivity (λ) was measured with a custom-built guarded hot plate device (protected zone: 50 mm x 50 mm, measuring zone: 25 mm x 25 mm) specifically designed to measure small low λ samples (Figure S1) [58]. The thermal conductivity was determined from monolithic square-shaped plates (SCD plates around 50 mm x 50 mm x 10 mm, APD plates around 70 mm x 70 mm x 10 mm) after

preconditioning at 30% relative humidity (RH) and 25 °C for at least 24 h. Thermogravimetric analysis was carried out using a Netzsch TGA 209 F1 instrument in reconstituted air (80% v/v N_2 and 20% v/v O_2), from 30 °C to 900 °C with a heating rate of 20 °C/min.

The mechanical properties were evaluated on cylindrical samples (15 mm diameter, 20–30 mm high) using a universal mechanical testing setup (Zwick/Z010, Zwick/Roell, Germany) to apply uniaxial compression with a 10kN force transducer (KAP-S, AST Gruppe GmbH, Germany) at a rate of 1 mm/min up to 80% strain in a controlled environment (23 °C and 50% RH). The elastic moduli were calculated from the linear region of the stress-strain curves (typically between 1 and 3% strain).

3. Results and discussion

3.1 Parameters affecting gelation and reaction mechanism

The main parameters that affect gelation are temperature and urea concentration: gelation only occurs for reaction temperatures of at least 80 °C and urea/d-glucosamine molar ratios of at least 4 to 1 (Tables S2 and S3). The effect of temperature is particularly striking: no gelation is observed at 70 °C, even after 48 h, whereas a strong gel that could be processed to an aerogel was obtained after just 5 h at 80 °C. The 80 °C required for gelation is consistent with the decomposition temperature of urea in aqueous solution for the two possible mechanisms, through hydrolysis [59–64] and/or through an isocyanate intermediate (Figure 2) [65,66]. Note also that the thermal decomposition of urea represents the onset of the formation of ammonia, where the former is responsible for the neutralization of the acidic sol medium previously mentioned in the text. Mechanistically we are not able to discern which of the proposed reaction mechanisms dominates during the aerogel synthesis, primarily because of the short-lived nature and correspondingly small effective concentrations of the intermediates. The results discussed above were obtained for a chitosan concentration of 10% m/v, but for the optimum conditions (80 °C, urea/d-glucosamine=6/1, 24h), gelation was observed for all investigated chitosan loadings (3, 5, 8, 10, 12 % m/v). The effect of protonation of chitosan in the solution, i.e. the concentration of HCl, was also investigated (Table S4), but all data in the remainder of this manuscript correspond to a degree of protonation of 180%. Note that chitosan depolymerizes under these conditions through the hydrolysis of the glycosidic bonds [67–69], therefore dissolution temperatures and times need to be kept constant to obtain consistent results. The dissolution of different concentrations of HW chitosan in different acids was also investigated, without success (Table S6). Note that the experiments above were carried out with chitosan with high molecular weight (310'000 – 375'000 g/mol) and that no gelation was observed with chitosan with medium (190'000-310'000 g/mol) and low (50'000–190'000 g/mol) molecular weight.
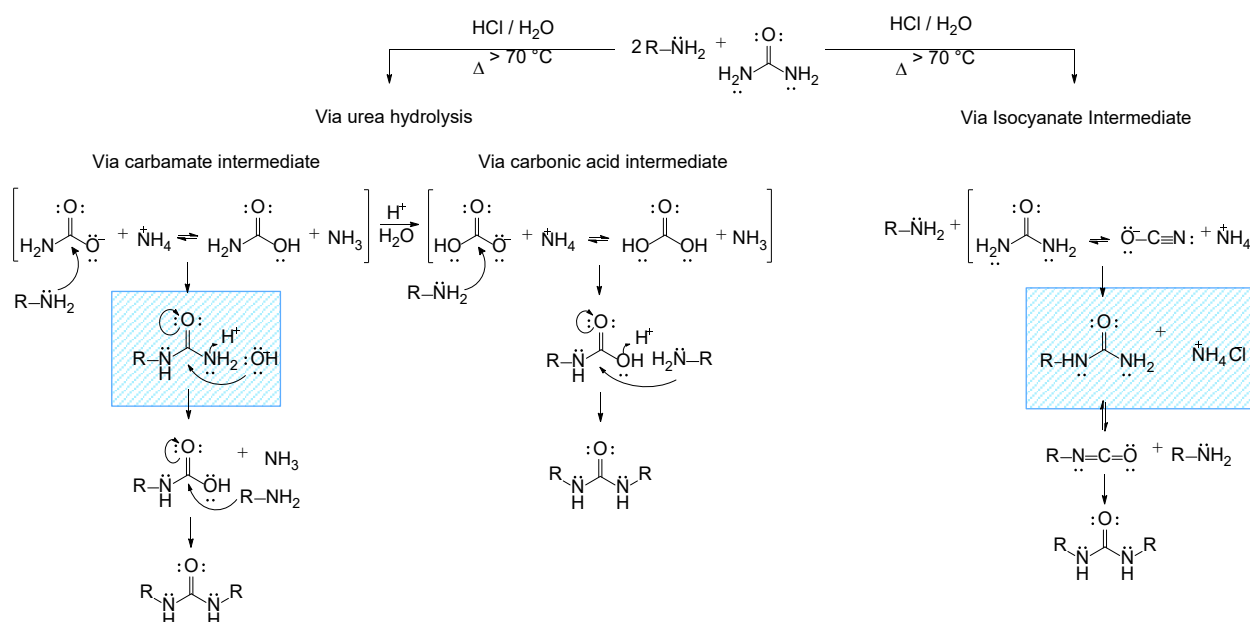
Figure 2. Possible reaction mechanisms for the formation of end-capping ureido groups (dominant species) and, possibly, cross-linking ureylene groups (minor species). The full decomposition of urea with water into CO_2 and NH_3 is not shown.

3.2 Aerogel chemistry and structure formation

Solid-state NMR spectroscopy

The ^1H-^{13}C CP MAS NMR spectrum of the chitosan-urea aerogel displays all the signatures expected for chitosan with a high degree of deacetylation (Figure 3a). Cross polarization spectra are not inherently quantitative because the relative peak intensities are modified by variable relaxation times and cross polarization efficiencies. Nevertheless, the reasonable agreement between the nominally expected (1.0/1.0/2.0/1.0/1.0) and measured (1.0/1.2/2.3/1.1/0.9) peak areas for C1, C2, C3+C5, C4 and C6 (Table S7) indicates that, for these samples and with these experimental conditions, the peak areas provide a reasonable approximation of the carbon abundances. The normalized intensities of the C7 (0.22) and C8 (0.23) bands indicate a degree of acetylation of around 23%. The normalized intensity of 0.77 of the C9 band, assigned to the C=O group of end-capping ureido groups, indicates that, within uncertainty, all of the deacetylated amino groups have reacted with urea to form ureido groups, i.e. few to no primary amino groups remain on the chitosan backbone. The presence of abundant end-capping ureido groups and the absence in the spectra of cross-linking urea groups is not unexpected. Because of the large urea excess at which the reaction is carried out (6:1 molar urea:d-glucosamine ratio), only 3% of ureylene cross-links would be expected based on a simple simulation that assumes equal kinetic rate constants for the end-capping (first step) and cross-linking (second step) reactions (Fig. S5). However, a parallel ongoing study in our laboratory on the reaction between ethanolamine and urea indicates that the probability of the ureylene cross-linking reaction is much lower than that of the ureido end-capping reaction. Thus, the 3% estimate represents an upper bound concentration of crosslinks. Because of the high molecular weight of chitosan, possible cross-links could still be expected to have a substantial effect

7

on gelation and structure formation, even at (very) low concentration. In other words, only few crosslinks would be needed to increase viscosity and promote gelation.
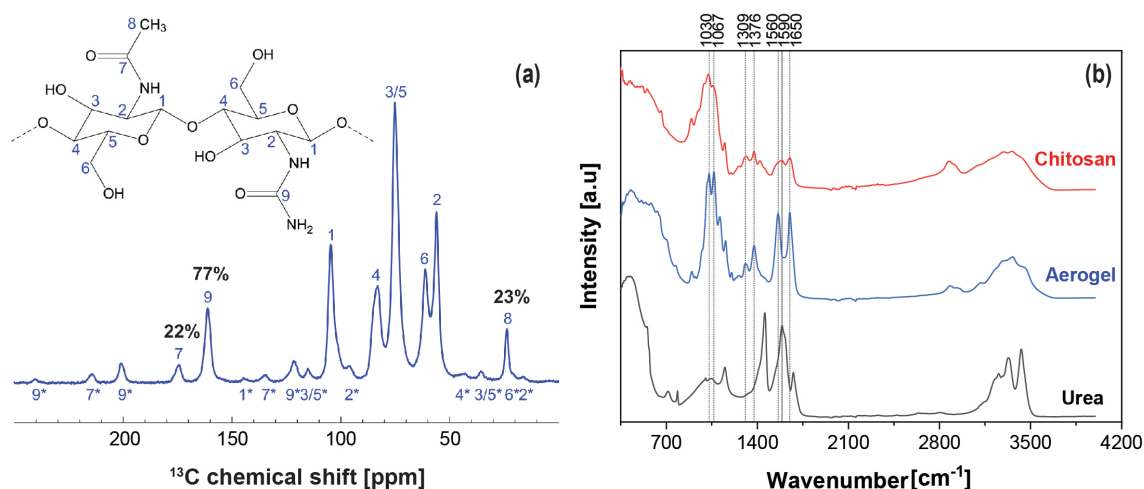

Figure 3. (a) Solid-state CP-MAS ^{1}H-^{13}C NMR spectrum of chitosan-urea aerogel (GA067). Peak assignments are illustrated with a fragment of chitosan; peaks labeled with an asterisk (*) are spinning sidebands. The relative intensity of the acetyl groups (C7/C8), including spinning sidebands and normalized to the total intensity of the C1 band, amounts to 22/23%. The relative intensity of ureido (C9) groups is 77%. (b) ATR-FTIR spectra of pure chitosan, aerogel and urea.

FT-IR spectroscopy

The FTIR spectrum of the urea-modified chitosan aerogel closely resembles that of neat chitosan (Figure 3b), apart from distinct changes in intensity and peak position in the 1550 to 1700 cm^{-1} region. Neat chitosan has two peaks in this region, one at 1590 cm^{-1} was assigned to the –NH$_2$ groups and one at 1650 cm^{-1} related to the acetyl group, i.e. –NHC(O)CH$_3$. The vibrational band of the -NH$_2$ groups at 1590 cm^{-1} is absent from the chitosan aerogel spectrum, but the urea-modified chitosan aerogels display two peaks in this region, at 1650 cm^{-1} and 1560 cm^{-1} typical for amide I and amide II vibrations, i.e. from the –NHC(O)NH$_2$ groups, that are too intense to arise entirely from the acetyl amide bands from the original chitosan. The experimental peak positions should not be over-interpreted as the bands are the sum of at least two overlapping sets of peaks (residual acetyl and newly formed ureido groups). Nevertheless, the relatively low frequency of the carbonyl stretching vibration (1650 cm^{-1}) is indicative of moderate to strong hydrogen bonding as a result of the delocalization of electrons in the π-bonds [70]. Compared to the neat chitosan spectrum, the peak at 1422 cm^{-1} related to CH$_2$ bending disappears in the aerogel spectrum and the peak assigned to C-H bending at 1376 cm^{-1} and to a lesser extent also the peak at 1309 cm^{-1} from C-N stretching (amide III) are more intense. The overlapping vibrational bands ascribed to C-O at 1030 and 1067 cm^{-1} display as two well-defined peaks in the aerogel spectrum. The vibrational bands of the O3-H and O6-H appear at relatively low frequencies in the aerogel spectrum (3361 cm^{-1} and 3453 cm^{-1}, respectively), indicating relatively strong hydrogen bonding. The complete peak assignments is listed in Table S8.

Structure formation

The change from a clear solution to a white gel during aging and gelation (at 80°C) indicates that larger aggregates that scatter visible light have formed during gelation, i.e. before solvent exchange and drying. Aggregation can be related to multiple effects (Figure 1), namely i) ammonia released during urea decomposition neutralizes the acid and reduces chitosan solubility [60], ii) the grafting of ureido groups onto the chitosan backbone, which changes the solvent-chitosan and chitosan-chitosan interactions, and enables the establishment of a "ureido" based hydrogen bonding network, and iii) the actual crosslinking of chitosan by ureylene moieties. The change in pH alone is not sufficient to explain the structure formation here, since chitosan gelation through the addition of base is generally reversible [37,49,71], which is not the case in our system: no dissolution of mass loss were observed after immersion of the urea-modified hydrogels in a pH2 HCl solution for 24 hours. In addition, gels produced by base addition to acidic chitosan solutions are mechanically much weaker than those prepared here. Thus, the microstructure and properties of the gels and aerogels produced here must be strongly linked to either or both of the remaining mechanisms, that is grafting of ureido groups and cross-linking with ureylene groups.

3.3 Shrinkage, density, humidity uptake, thermal stability and thermal conductivity

Shrinkage and density

The importance of shrinkage of (bio)polymer aerogels during processing has been highlighted recently [72]. For all investigated processing steps (solvent exchanges, drying), there is a clear, inverse correlation between chitosan concentration and linear shrinkage (Figure 4a), as is typical for most aerogel systems and simply because the increased mechanical strength of more concentrated gels enables them to better withstand the stresses during processing. Compared to other biopolymer aerogel systems [72], the solvent exchange into ethanol and heptane leads to only a moderate linear shrinkage (between 2 and 12% for 3% m/v chitosan, and between 2 and 4% for 12% m/v chitosan), despite the very low solubility of chitosan in ethanol and heptane. We interpret this as further proof that the microstructure/aggregation of chitosan occurred before washing and solvent exchange steps, i.e. during gelation and aging. Shrinkage is more pronounced after drying. For SCD, the higher linear shrinkage (20%) at low concentrations results in a relatively flat dependence of density on chitosan concentration, but the lowest densities are observed for the lowest chitosan concentrations (Figure 4b). In the case of APD, we see much higher shrinkage and also the dependence of shrinkage on chitosan concentration is even more extreme. The apparent density dependence is a complex function of chitosan concentration with the lowest APD densities being observed for the highest chitosan concentrations, contrary to the SCD samples. The faster drying at higher APD temperatures reduces the time for which the gels are exposed to drying induced capillary forces. The lower densities after APD at 65 °C, compared to room temperature, seem to confirm this hypothesis.
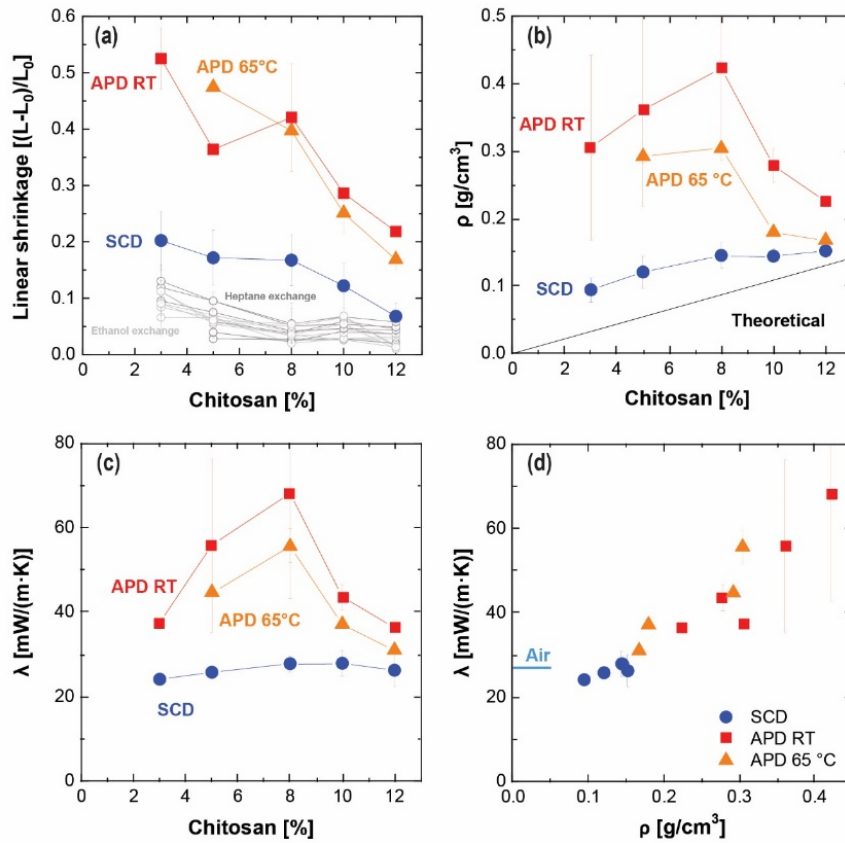
9

Figure 4. (a) Linear shrinkage as a function of chitosan concentration. (b) Density dependence on chitosan concentration. (c) Thermal conductivity versus chitosan concentration. (d) Thermal conductivity versus density.

Thermal conductivity

The thermal conductivity λ (Figure 4c) strongly correlates with aerogel density: The SCD and APD (RT/65°C) data define a single monotonously increasing function of aerogel density (Figure 4d). No minimum in thermal conductivity is observed at intermediate densities, as is typical for many aerogel systems [1,73], but the lowest thermal conductivity is observed for the lowest density samples. This indicates the important contributions of the solid conduction in shaping the density dependence of thermal conductivity over the investigated density range (0.094-0.423 g/cm^3). Thermal conductivities as low as 24.1 mW/(m·K) are reached for the lowest density SCD-dried aerogels (Table 1) and even lower conductivities were measured for aerogels processed at 90 °C (22.1 mW/(m·K), Table S3). These values are well below that of standing air (26 mW/(m·K) and much lower than for conventional insulation materials (e.g. mineral wool or EPS with ~33 mW/(m·K)), indicating that the gas phase conduction is at least partially suppressed through the Knudsen effect because of the mesoporous pore network. Presumably, the gas phase conduction is even lower for the higher density aerogels with their smaller pores, but this effect is masked by the higher solid phase conduction. The APD aerogels display higher densities and thermal conductivities, but still in line with those of conventional insulation materials. The

lower densities for APD at 65 °C (compared to room temperature) lead to lower thermal conductivities: a value of 30.9 mW/(m·K) is achieved for the lowest density APD-dried aerogel (Table 1).

Moisture uptake and thermal stability

The chitosan-urea aerogels are hydrophilic and display very substantial water uptake, even at low relative humidity (Figure S2). For example, the 10% SCD chitosan samples display a humidity uptake of 2.4, 6.1 and 6.3% w/w after exposure to 30% relative humidity for 1 hour, 1 day, and 14 days, respectively. The APD samples show a similar behaviour. The relatively high moisture uptake is expected to negatively affect the thermal conductivity as lambda is known to increase through water uptake [74]. Hydrophobization of the chitosan aerogels may help to decrease the thermal conductivity and/or reduce its dependence on relative humidity, but only a single study has reported on the hydrophobization of mesoporous chitosan aerogels [32,45]. Generally the durable hydrophobization of biopolymer based aerogels remains a big challenge for the community. In addition, most hydrophobization protocols seem to only improve the (liquid) water contact angle while leaving humidity uptake relatively unaffected [75].

The humidity uptake is reflected in the weight loss (2.6 to 5.5%) upon drying as seen during thermogravimetry between 50 and 150 °C for all investigated materials: chitosan starting material, SCD and APD aerogels (Figure 5a). A more pronounced, rapid loss of mass of 65 to 70% is observed with a maximum rate at ~350 °C, which is higher than for neat chitosan (~315°C), but with a lower onset temperature (200 °C). The good high temperature stability as observed by TGA is consistent with the aerogel's behaviour when exposed to a flame (Figure 5b, Figure S4, S5). Both the SCD and APD aerogels char and carbonize rather than burn when exposed to a flame, and retain their structural integrity throughout. Once the heat source is removed, the glow disappears immediately. The fire retarding properties of chitosan are well known, particularly in combination with phosphate chemistry [76,77]. The nature of the degradation products after flame exposition was not investigated here. The decomposition of urea and urea derivatives is complex. In general, high temperature decomposition of urea generates isocyanic acid and biuret, which can be converted to CO_2 and NH_3, or back to urea, respectively. [78,79]
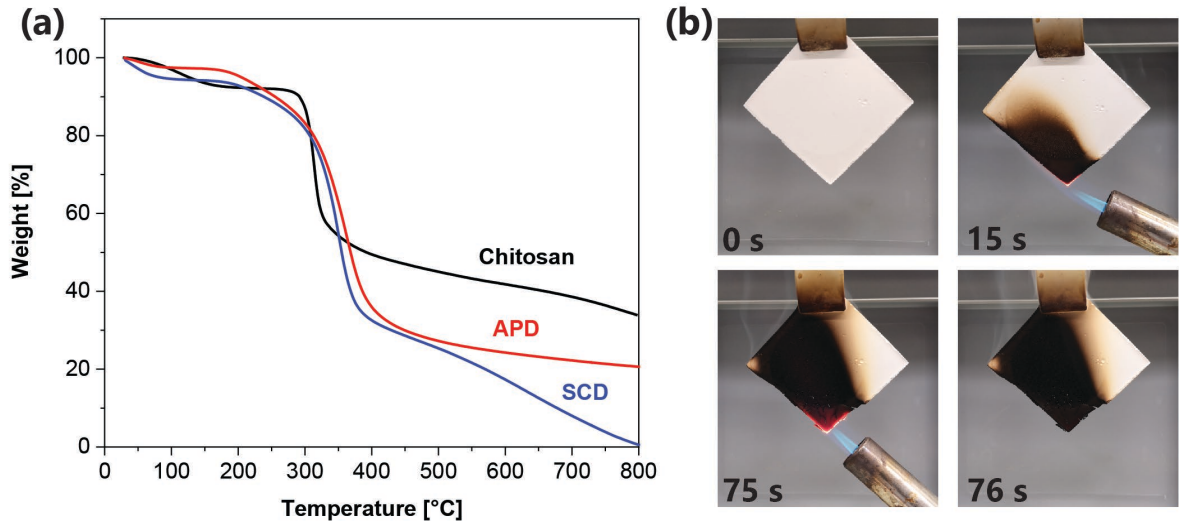
Figure 5. (a) Thermogravimetry of neat chitosan and chitosan-urea aerogels (SCD and APD, 10% m/v chitosan); the analysis was conducted in reconstituted air. (b) Fire behavior of APD chitosan-urea aerogel (10% m/v chitosan).

Table 1. Chitosan-urea aerogel properties. Additional properties are listed in Table S10.

	Chit. [wt%]	ρ [g/cm^3]		Porosity [%]		V_{pore} [cm^3/g]		$V_{pore\ BJH\ Ads.}$ [cm^3/g]		S_{BET} [m^2/g]		C - value		D_{pore} [nm]		$D_{pore\ BJH\ Ads.}$ [nm]		λ [mW/(m·K)]	
		Av.	SD	Av.	SD	Av.	SD	Av.	SD	Av.	SD	Av.	SD	Av.	SD	Av.	SD	Av.	SD
SCD	3	0.094	0.018	91.8	1.7	9.9	1.9	0.8	0.1	165	20	144	9	245	68	22.5	2.1	24.1	0.9
	5	0.121	0.024	90.0	2.0	8.1	2.0	0.8	0.1	172	17	173	40	190	51	21.7	0.9	25.7	0.2
	8	0.145	0.021	88.0	1.7	6.4	1.0	0.7	0.0	159	3	140	13	160	22	20.8	0.9	27.8	1.9
	10	0.144	0.013	87.5	1.1	6.0	0.6	0.7	0.1	160	8	154	30	152	21	20.2	1.4	27.9	2.9
	12	0.152	0.011	87.3	0.9	5.9	0.5	0.7	0.0	167	7	124	4	141	10	19.4	0.5	26.2	3.8
APD dried at RT	3	0.305	0.138	79.4	9.5	4.9	2.2	0.9	0.1	150	12	119	12	131	51	25.3	0.8	37.5	0.0
	5	0.361	0.142	66.3	11.1	2.8	1.2	0.7	0.0	127	14	117	12	87	26	25.1	1.1	62.5	19.8
	8	0.423	0.138	65.1	11.3	2.7	1.2	0.5	0.1	83	16	147	31	149	95	26.8	2.2	68.1	25.1
	10	0.278	0.026	75.9	0.5	3.4	0.1	0.7	0.0	134	0	125	8	102	3	22.3	0.6	41.6	3.1
	12	0.225	0.005	81.4	0.4	4.4	0.1	0.5	0.1	106	20	156	51	173	35	20.3	1.2	36.3	0.3
APD dried at 65 °C	5	0.292	0.008	74.4	1.2	2.6	0.1	1.0	0.0	210	0	118	0	49	3	21.2	0.3	44.5	1.0
	8	0.304	0.000	76.3	0.0	2.9	0.0	0.4	0.4	174	2	135	4	65	0	21.2	0.7	55.6	4.0
	10	0.180	0.007	85.0	0.4	4.9	0.2	0.9	0.0	228	7	115	6	108	0	21.3	0.7	37.0	0.8
	12	0.167	0.006	86.2	0.4	5.3	0.2	1.0	0.0	227	5	139	16	94	6	19.2	0.1	30.9	1.0

SD: standard deviation from N measurements on N different samples ($\sqrt{\frac{\sum(x-\bar{x})}{N}}$). The number of measurements used to calculate the average and SD is listed in Table S10.

V$_{pore}$ calculated from envelope and skeletal density: $V_{pore} = \frac{1}{\rho_{bulk}} - \frac{1}{\rho_{skeletal}}$

D$_{pore}$ calculated from V$_{pore}$ and surface area: $D_{pore} = \frac{4 \cdot V_{pore}}{S_{BET}}$

3.4 Microstructure

The chitosan-urea aerogels presented here display a particle-network type microstructure (Figure 6), which is somewhat unusual as (nano) fibrillary structures are more common for chitosan aerogels [31,55]. Both the SCD and APD aerogels consist of linked particles of ~50 nm in diameter (ranging from 20 to 90 nm), corresponding to a theoretical surface area of ~75 m^2/g (ranging from 190 to 40 m^2/g), calculated under the assumption of spherical particles and a skeletal density of 1.59 g/cm^3 (Supporting Information) and consistent with those determined by nitrogen sorption analysis (80-230 m^2/g, Table 1). The material displays local density variations between regions with predominantly mesopores domains separated by macropores. The largest observed pores are 150 and 650 nm in diameter for the SCD (Fig 6a, 6c) and APD (Fig. 6b,6d) dried aerogels, respectively. The higher macroporosity for the APD samples is related to platelet-like structures that most likely were formed by a partial structural collapse during evaporative drying. (Fig.6b, 6d)
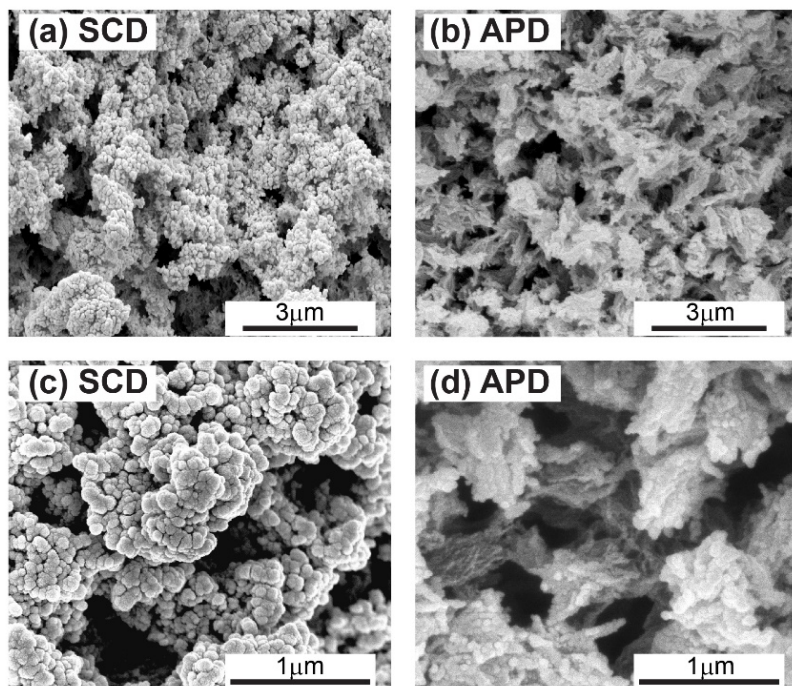

Figure 6. SEM images of chitosan-urea aerogels. (a) SCD aerogel (30'000x). (b) APD aerogel (30'000x). (c) SCD aerogel (100'000x). (d) APD aerogel (100'000x). SCD and APD images are from gels prepared from a 5% m/v and 10% m/v chitosan solution, respectively.

Nitrogen sorption analysis further confirms the presence of significant surface area and mesoporosity (Fig. 7). All samples (SCD, APD RT and APD 65 °C) display nitrogen sorption isotherms with a type IV hysteresis, according to the IUPAC classification. The strong increase of the volume of N_2 adsorbed in the capillary condensation regime, combined with a narrow desorption hysteresis loop is characteristic of the material's mesoporosity. (Fig 7a, Fig S3). This can be also observed in the BJH pore size

distributions (Fig 7b, Fig S3), which are broad and include significant meso- and macroporosity for all samples. As is typical for aerogels, the BJH derived pore sizes are significantly lower than those derived from the envelope and skeletal density because of the inability for nitrogen sorption to sample larger pores, and the possible deformation of the aerogels upon desorption [57]. The APD samples dried at room temperature display the highest densities and lowest surface areas and significant scatter in both density and surface area (Fig. 7c). The APD samples dried at 65°C give more consistent results and have intermediate densities and the highest surface areas. Finally, the SCD aerogels display the lowest densities and intermediate surface areas. The surface areas of the APD chitosan aerogels are in the same range as those for SCD, particularly for those dried at 65°C (Fig. 7c), in contrast to light-weight cellulose xerogels, where APD leads to a substantial decrease in surface area [80].
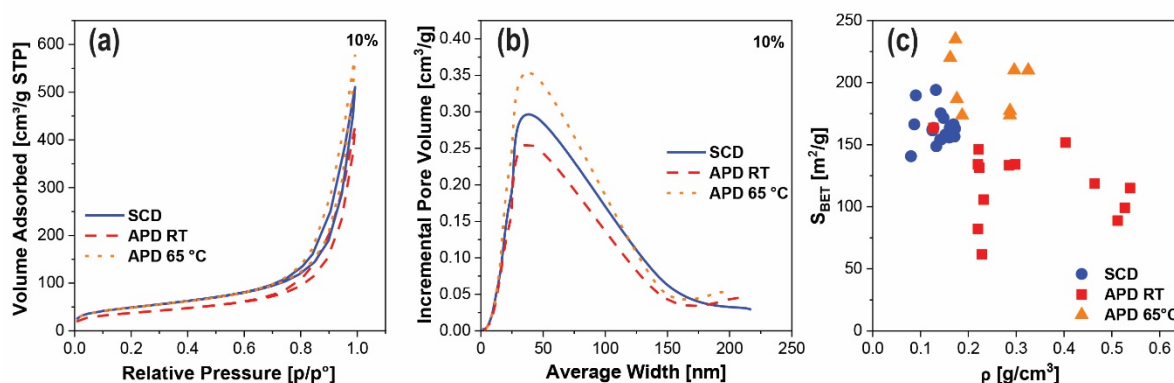

Figure 7. Nitrogen sorption data. (a) Nitrogen sorption isotherms of 10% chitosan sample; (b) BJH desorption plots of 10% chitosan sample; (c) Surface area as a function of density for all different chitosan concentrations. Isotherms and pore size distributions for other chitosan concentrations are shown in Figure S3.

3.5 Mechanical properties and machinability

Regardless of chitosan concentration, all aerogels prepared in this study sustain compression stress without rupture up to at least 80%, and display relatively high E moduli and σ_{80} (Fig. 8). Not surprisingly, the best mechanical performance is found for the densest aerogels, prepared with 12% chitosan, with a compressive E modulus of 11.6 MPa (Table 2). The samples are not brittle and no dust release is observed. The samples can be compressed up to 80% strain without rupture, with a σ_{80} as high as 17.9 MPa (for 12% chitosan). However, the compression is mostly irreversible, even at smaller deformations, and the samples appear as cohesive, compressed, flattened disks after testing and material properties such as density and thermal conductivity will start to deteriorate at much lower loads than the reported σ_{80} values (Fig. 8c). As is typical for aerogels, the E-modulus displays a power-law dependence on density $E \sim \rho^{\alpha}$, with $\alpha=2.6$, i.e. a linear dependence on density on a log-log plot (Figure 8b). Overall, the mechanical properties are in line with those observed for other biopolymer and biopolymer-silica hybrid aerogels [6,75,81–84], but much better than traditional silica aerogels [73]. Remarkably, and in stark contrast to many other aerogel systems, both the SCD and APD aerogels are non-brittle and machinable with standard

tools. A variety of samples prepared from different chitosan concentrations and dried by both SCD and APD were machined by drilling and sawing. Systematic tests were carried out only for samples prepared from 10%, both for SCD and APD. The samples resisted these tests without fracture (Fig. 9).
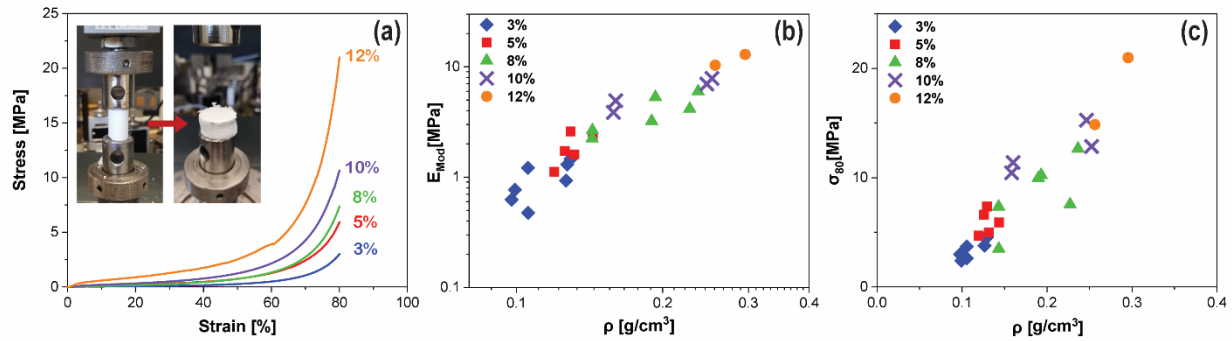

Figure 8. a) Stress-strain curves of SCD samples for different chitosan concentrations. b) E modulus as a function of density (log-log plot). c) Stress at 80% strain.

Table 2. Mechanical properties of chitosan aerogels.

Chit. [%]	ρ [g/cm^3]		E [MPa]		σ_{80} [MPa]		N
	Av.	SD	Av.	SD	Av.	SD	
3 %	0.113	0.013	1.0	0.3	3.5	0.8	7
5 %	0.130	0.008	1.9	0.5	5.9	1.0	5
SCD Aerogels 8 %	0.189	0.036	3.9	1.4	8.5	2.9	6
10 %	0.204	0.045	5.9	1.6	12.5	1.8	4
12 %	0.276	0.020	11.6	1.3	17.9	3.1	2

SD: standard deviation from N measurements on N different samples ($\sqrt{\frac{\sum(x-\bar{x})}{N}}$)
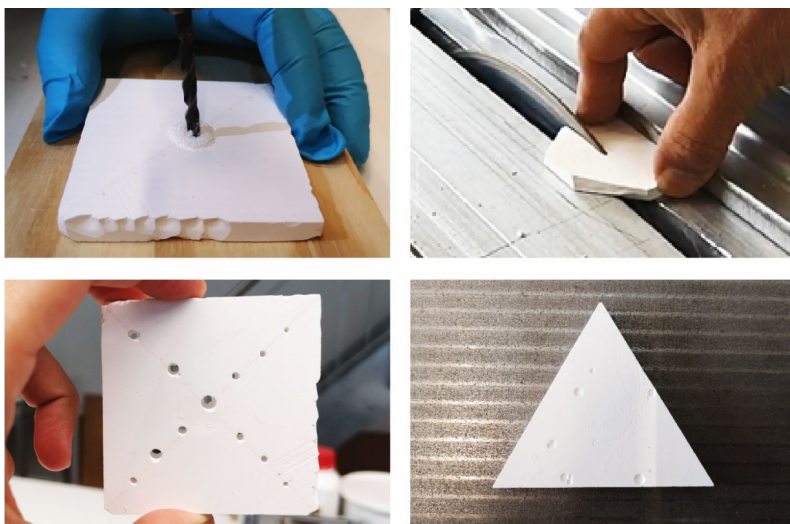
Figure 9. Machinability of the 10% chitosan aerogels and xerogels subjected to drilling and sawing.

3.6 Comparison to other biopolymer aerogels

Biopolymer aerogels prepared by freeze drying (FD) most often display low surface areas and (very) low envelope densities, whereas those prepared by SCD display higher surface areas and a wide range in density (Fig. 10a). Compared to other biopolymer aerogels prepared by SCD, the chitosan-urea SCD aerogels display moderately high surface areas and rather high envelope densities. Far fewer data have been reported for biopolymer aerogels prepared by APD, but the chitosan-urea APD aerogels presented here display relatively high surface areas, particularly those dried at 65°C (Fig. 10a).

The last few years have seen a rapid increase in reported thermal conductivity data for biopolymer aerogels (Fig. 10b). Biopolymer aerogels with thermal conductivities below 20 mW/(m·K) cluster around densities of 0.100 g/cm^3 and surface areas above 300 m^2/g, and have all been prepared by supercritical drying. A minimum in thermal conductivity at intermediate densities is typical for aerogels: at higher densities, heat conduction through the solid skeleton increases rapidly; at low densities, there is not enough material available to partition the space into small enough pores to suppress the gas phase conduction by the Knudsen effect [1]. Notable examples of superinsulating aerogels in this intermediate density range include pectin [85], cellulose [86] and chitosan aerogels [31]. The SCD chitosan-urea aerogels from this study display thermal conductivities below 26 mW/(m·K) (standing air) and well below 30-35 mW/(m·K) (mineral wool, EPS), indicative of a partial suppression of the gas phase conduction and consistent with the estimated pore sizes (Fig. 10b). The thermal conductivity is, however, above 20 mW/(m·K), most likely because of the relatively high densities, the only moderately high surface areas and the only moderately small pore sizes. Thus, a reduction in thermal conductivity will require further optimization towards lower densities and/or higher surface areas.

The APD chitosan-urea aerogels are the first APD biopolymer aerogels for which thermal conductivity data are reported. They display thermal conductivities as low as 30.9 mW/(m·K), i.e. lower than natural insulation materials (e.g. wool or stray) and at the lower end of what is possible with conventional, air-filled insulation materials (e.g. mineral wool or EPS), albeit with very different densities and pore structures. Given the estimated pore size, the gas phase conduction is expected to be partially reduced for the APD chitosan-urea aerogels, but not for conventional insulators. However, these benefits are negated by the higher densities of 0.167 to 0.304 g/cm^3 compared to 0.015 to 0.050 g/cm^3 for conventional insulators. With these similar thermal conductivity values, APD chitosan-urea aerogels are not competitive with inexpensive, conventional insulation products. However, the APD chitosan-urea aerogels provide the first demonstration that high-performance biopolymer aerogel insulation produced by ambient pressure drying may be within reach, a feat that for now remains exclusive to silica aerogel.
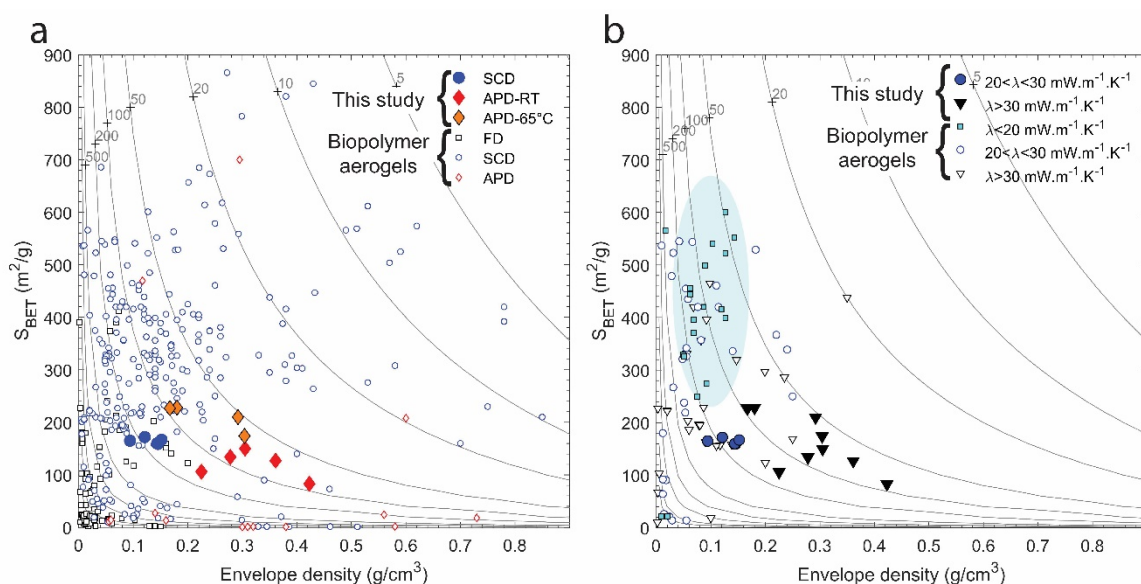

Figure 10. Comparison to other biopolymer aerogels. a) Surface area versus envelope density, separated by drying technique. b) Surface area versus envelope density, separated by thermal conductivity. The contour lines denote average pore sizes (in nm) calculated from density and surface area, assuming cylindrical pores. Data source: 2018 review paper [6] augmented with more recent literature data (Table S11).

4. Conclusions

Sustainable biopolymer aerogels are produced from renewable, waste-derived chitosan and urea as a "green" modifier. The reaction of chitosan with urea in an aqueous medium grafts abundant ureido groups onto the chitosan backbone, possibly in addition to minor cross-linking ureylene. This modification alters the chitosan-chitosan and chitosan-solvent interactions and leads to irreversible gelation, without the need for toxic cross-linkers such as formaldehyde. The urea-modified chitosan aerogels display exceptional mechanical properties (no brittle rupture, easy machinability) and moderately high surface area and mesoporosity. The thermal conductivity reaches values below that of

standing air or conventional insulation materials. We also find a remarkable high-temperature stability and self-extinguishing behaviour during simplified fire testing. The simple and non-toxic synthesis process and excellent machinability broaden their application potential, for example towards insulation and biomedical applications. Remarkably, this class of chitosan-urea gels can be transformed into mesoporous, monolithic aerogels by evaporative drying. The ability to produce monolithic, mesoporous chitosan aerogels by ambient pressure drying, a first in the field of biopolymer aerogels, and represents an important milestone towards cost-effective biopolymer aerogel production.

Acknowledgments

Supporting Information

Pdf file: Effect of different reagent concentrations, chitosan: urea ratio, temperature, time, HCl concentration, chitosan molecular weight on gelation and aerogel properties. Chitosan solubility in different acids. Tables with peak positions and assignment of solid-state NMR and FTIR spectra. Calculation of the theoretical relationship between surface area and particle size. Humidity uptake and nitrogen sorption data for different chitosan concentrations. Flame test on SCD sample. Thermal conductivity device. Theoretical estimate of ureylene versus ureido concentration.

Excel file: Table S11. Recent biopolymer aerogel data.

TOC text

Biopolymer aerogels are a sustainable alternative to commercially available silica aerogel. Modification of chitosan with urea enabled the production of chitosan aerogels with excellent mechanical properties, thermal conductivities below that of air, and exceptional fire properties. In contrast to previous studies, no toxic cross-linkers were necessary and drying without supercritical CO_2 was feasible, a milestone towards industrial production.

TOC keyword

Biopolymer aerogels

Table of Contents
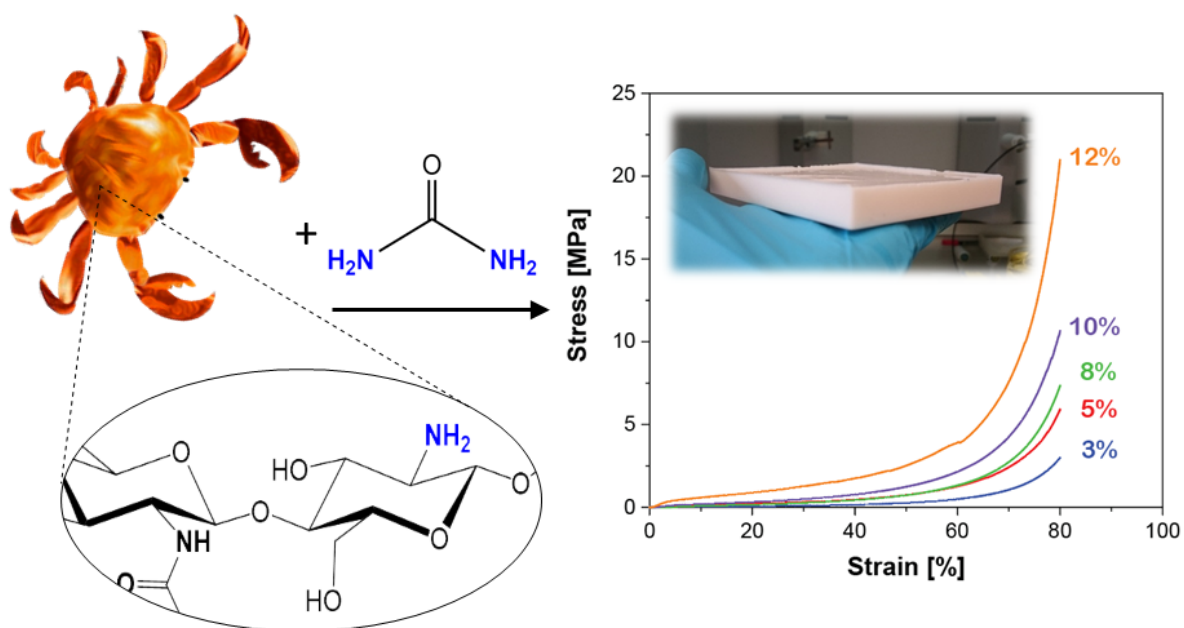
References

(1) Hüsing, N.; Schubert, U. Aerogels—Airy Materials: Chemistry, Structure, and Properties. *Angew. Chemie Int. Ed.* **1998**, *37* (1/2), 22–45. https://doi.org/10.1002/1521-3773(19980202)37:1/2<22::AID-ANIE22>3.3.CO;2-9.

(2) Aegerter, M.; Leventis, N.; Koebel, M. *Aerogels Handbook*; Aegerter, M. A., Leventis, N., Koebel, M. M., Eds.; Springer New York Dordrecht Heidelberg London: New York, NY, 2011. https://doi.org/10.1007/978-1-4419-7589-8.

(3) Koebel, M.; Rigacci, A.; Achard, P. Aerogel-Based Thermal Superinsulation: An Overview. *J. Sol-Gel Sci. Technol.* **2012**, *63* (3), 315–339. https://doi.org/10.1007/s10971-012-2792-9.

(4) Baetens, R.; Jelle, B. P.; Gustavsen, A. Aerogel Insulation for Building Applications: A State-of-the-Art Review. *Energy Build.* **2011**, *43* (4), 761–769. https://doi.org/10.1016/j.enbuild.2010.12.012.

(5) Prakash, S. S.; Brinker, C. J.; Hurd, A. J.; Rao, S. M. Silica Aerogel Films Prepared at Ambient Pressure by Using Surface Derivatization to Induce Reversible Drying Shrinkage. *Nature* **1995**, *374* (6521), 439–443. https://doi.org/10.1038/374439a0.

(6) Zhao, S.; Malfait, W. J.; Guerrero-Alburquerque, N.; Koebel, M. M.; Nyström, G. Biopolymer Aerogels and Foams: Chemistry, Properties, and Applications. *Angew. Chemie - Int. Ed.* **2018**, *57* (26), 7580–7608. https://doi.org/10.1002/anie.201709014.

(7) Yan, N.; Chen, X. Sustainability: Don't Waste Seafood Waste. *Nature* **2015**, *524* (7564), 155–157. https://doi.org/10.1038/524155a.

(8) Hülsey, M. J. Shell Biorefinery: A Comprehensive Introduction. *Green Energy Environ.* **2018**, *3* (4), 318–327. https://doi.org/10.1016/j.gee.2018.07.007.

(9) Risen, W. M.; Ji, S.; Hu, X.; Zhang, R. AEROGEL MATERIALS AND DETECTORS, LIQUID AND GAS ABSORBING OBJECTS, AND OPTICAL DEVICES COMPRISING SAME. US6303046B1, 2001.

(10) Alhwaige, A. A.; Agag, T.; Ishida, H.; Qutubuddin, S. Biobased Chitosan Hybrid Aerogels with Superior Adsorption: Role of Graphene Oxide in CO2 Capture. *RSC Adv.* **2013**, *3* (36), 16011–16020. https://doi.org/10.1039/c3ra42022a.

(11) Varma, A. J.; Deshpande, S. V.; Kennedy, J. F. Metal Complexation by Chitosan and Its Derivatives: A Review. *Carbohydr. Polym.* **2004**, *55* (1), 77–93. https://doi.org/10.1016/j.carbpol.2003.08.005.

(12) Guibal, E. Interactions of Metal Ions with Chitosan-Based Sorbents: A Review. *Sep. Purif. Technol.* **2004**, *38* (1), 43–74. https://doi.org/10.1016/j.seppur.2003.10.004.

(13) Zhang, S.; Feng, J.; Feng, J.; Jiang, Y. Formation of Enhanced Gelatum Using Ethanol/Water Binary Medium for Fabricating Chitosan Aerogels with High Specific Surface Area. *Chem. Eng. J.* **2017**, *309*, 700–707. https://doi.org/10.1016/j.cej.2016.10.098.

(14) Wang, J.; Zhou, Q.; Song, D.; Qi, B.; Zhang, Y.; Shao, Y.; Shao, Z. Chitosan–Silica Composite Aerogels: Preparation, Characterization and Congo Red Adsorption. *J. Sol-Gel Sci. Technol.* **2015**, *76* (3), 501–509. https://doi.org/10.1007/s10971-015-3800-7.

(15) Chang, X.; Chen, D.; Jiao, X. Chitosan-Based Aerogels with High Adsorption Performance. *J. Phys. Chem. B* **2008**, *112* (26), 7721–7725. https://doi.org/10.1021/jp8011359.

(16) Mahaninia, M. H.; Wilson, L. D. Cross-Linked Chitosan Beads for Phosphate Removal from Aqueous Solution. *J. Appl. Polym. Sci.* **2015**, *133* (5), n/a-n/a. https://doi.org/10.1002/app.42949.

(17) Chtchigrovsky, M.; Primo, A.; Gonzalez, P.; Molvinger, K.; Robitzer, M.; Quignard, F.; Taran, F. Functionalized Chitosan as a Green, Recyclable, Biopolymer-Supported Catalyst for the [3+2] Huisgen Cycloaddition. *Angew. Chemie Int. Ed.* **2009**, *48* (32), 5916–5920. https://doi.org/10.1002/anie.200901309.

(18) Kadib, A. El; Molvinger, K.; Cacciaguerra, T.; Bousmina, M.; Brunel, D. Chitosan Templated Synthesis of Porous Metal Oxide Microspheres with Filamentary Nanostructures. *Microporous*

Mesoporous Mater. **2011**, *142* (1), 301–307. https://doi.org/10.1016/j.micromeso.2010.12.012.

(19)   Frindy, S.; Primo, A.; Lahcini, M.; Bousmina, M.; Garcia, H.; El Kadib, A. Pd Embedded in Chitosan Microspheres as Tunable Soft-Materials for Sonogashira Cross-Coupling in Water–Ethanol Mixture. *Green Chem.* **2015**, *17* (3), 1893–1898. https://doi.org/10.1039/C4GC02175D.

(20)   Frindy, S.; Primo, A.; Ennajih, H.; el kacem Qaiss, A.; Bouhfid, R.; Lahcini, M.; Essassi, E. M.; Garcia, H.; El Kadib, A. Chitosan-Graphene Oxide Films and CO2-Dried Porous Aerogel Microspheres: Interfacial Interplay and Stability. *Carbohydr. Polym.* **2017**, *167*, 297–305. https://doi.org/10.1016/j.carbpol.2017.03.034.

(21)   Primo, A.; Quignard, F. Chitosan as Efficient Porous Support for Dispersion of Highly Active Gold Nanoparticles: Design of Hybrid Catalyst for Carbon–Carbon Bond Formation. *Chem. Commun.* **2010**, *46* (30), 5593. https://doi.org/10.1039/c0cc01137a.

(22)   Quignard, F.; Valentin, R.; Di Renzo, F. Aerogel Materials from Marine Polysaccharides. *New J. Chem.* **2008**, *32* (8), 1300. https://doi.org/10.1039/b808218a.

(23)   Kayser, H.; Müller, C. R.; García-González, C. A.; Smirnova, I.; Leitner, W.; Domínguez De María, P. Dried Chitosan-Gels as Organocatalysts for the Production of Biomass-Derived Platform Chemicals. *Appl. Catal. A Gen.* **2012**, *445–446*, 180–186. https://doi.org/10.1016/j.apcata.2012.08.014.

(24)   Hu, X.; Littrel, K.; Ji, S.; Pickles, D. G.; Risen, W. M. Characterization of Silica–Polymer Aerogel Composites by Small-Angle Neutron Scattering and Transmission Electron Microscopy. *J. Non. Cryst. Solids* **2001**, *288* (1–3), 184–190. https://doi.org/10.1016/S0022-3093(01)00625-1.

(25)   Yao, C.; Risen, W. M. Formation and Reaction of Metal-Containing Nanoparticles in Organic/Inorganic Hybrid Aerogels. *MRS Proc.* **2005**, *847*, EE5.10.1-EE.10.6. https://doi.org/10.1557/PROC-847-EE5.10.

(26)   Singh, J.; Dutta, P. K.; Dutta, J.; Hunt, A. J.; Macquarrie, D. J.; Clark, J. H. Preparation and Properties of Highly Soluble Chitosan-l-Glutamic Acid Aerogel Derivative. *Carbohydr. Polym.* **2009**, *76* (2), 188–195. https://doi.org/10.1016/j.carbpol.2008.10.011.

(27)   Wang, M.; Liu, X.; Ji, S.; Risen, W. M. A New Hybrid Aerogel Approach to Modification of Bioderived Polymers for Materials Applications. *MRS Proc.* **2002**, *702*, U3.5.1-U3.5.9. https://doi.org/10.1557/PROC-702-U3.5.1.

(28)   Zhao, S.; Xu, H.; Wang, L.; Zhu, P.; Risen, W. M.; William Suggs, J. Synthesis of Novel Chitaline-Silica Aerogels with Spontaneous Au and Ag Nanoparticles Formation in Aerogels Matrix. *Microporous Mesoporous Mater.* **2013**, *171*, 147–155. https://doi.org/10.1016/j.micromeso.2012.12.038.

(29)   Wang, R.; Shou, D.; Lv, O.; Kong, Y.; Deng, L.; Shen, J. PH-Controlled Drug Delivery with Hybrid Aerogel of Chitosan, Carboxymethyl Cellulose and Graphene Oxide as the Carrier. *Int. J. Biol. Macromol.* **2017**, *103*, 248–253. https://doi.org/10.1016/j.ijbiomac.2017.05.064.

(30)   Iglesias, C. L.; Barros, J.; Ardao, I.; Gurikov, P.; Monteiro, F. J.; Smirnova, I.; Lorenzo, C. A.; González, C. A. G. Jet Cutting Technique for the Production of Chitosan Aerogel Microparticles Loaded with Vancomycin. **2020**, 1–13. https://doi.org/10.3390/polym12020273.

(31)   Takeshita, S.; Yoda, S. Chitosan Aerogels: Transparent, Flexible Thermal Insulators. *Chem. Mater.* **2015**, *27*, 7569–7572. https://doi.org/10.1021/acs.chemmater.5b03610.

(32)   Takeshita, S.; Yoda, S. Translucent, Hydrophobic, and Mechanically Tough Aerogels Constructed from Trimethylsilylated Chitosan Nanofibers. *Nanoscale* **2017**, *9* (34), 12311–12315. https://doi.org/10.1039/C7NR04051B.

(33)   Zhao, S.; Malfait, W. J.; Jeong, E.; Fischer, B.; Zhang, Y.; Xu, H.; Angelica, E.; Risen, W. M.; Suggs, J. W.; Koebel, M. M. Facile One-Pot Synthesis of Mechanically Robust Biopolymer–Silica Nanocomposite Aerogel by Cogelation of Silicic Acid with Chitosan in Aqueous Media. *ACS Sustain. Chem. Eng.* **2016**, *4* (10), 5674–5683. https://doi.org/10.1021/acssuschemeng.6b01574.

(34)   El Kadib, A.; Bousmina, M. Chitosan Bio-Based Organic-Inorganic Hybrid Aerogel Microspheres.

Chem. - A Eur. J. **2012**, *18* (27), 8264–8277. https://doi.org/10.1002/chem.201104006.

(35)   Wang, Q. Z.; Chen, X. G.; Liu, N.; Wang, S. X.; Liu, C. S.; Meng, X. H.; Liu, C. G. Protonation Constants of Chitosan with Different Molecular Weight and Degree of Deacetylation. *Carbohydr. Polym.* **2006**, *65* (2), 194–201. https://doi.org/10.1016/j.carbpol.2006.01.001.

(36)   Raman, S. P.; Gurikov, P.; Smirnova, I. Hybrid Alginate Based Aerogels by Carbon Dioxide Induced Gelation: Novel Technique for Multiple Applications. *J. Supercrit. Fluids* **2015**, *106*, 23–33. https://doi.org/10.1016/j.supflu.2015.05.003.

(37)   Iglesias, N.; Galbis, E.; Valencia, C.; de-Paz, M. V.; Galbis, J. A. Reversible PH-Sensitive Chitosan-Based Hydrogels. Influence of Dispersion Composition on Rheological Properties and Sustained Drug Delivery. *Polymers (Basel).* **2018**, *10* (4). https://doi.org/10.3390/polym10040392.

(38)   Nilsen-Nygaard, J.; Strand, S. P.; Vårum, K. M.; Draget, K. I.; Nordgård, C. T. Chitosan: Gels and Interfacial Properties. *Polymers (Basel).* **2015**, *7* (3), 552–579. https://doi.org/10.3390/polym7030552.

(39)   Cho, J.; Heuzey, M. C.; Bégin, A.; Carreau, P. J. Physical Gelation of Chitosan in the Presence of β-Glycerophosphate: The Effect of Temperature. *Biomacromolecules* **2005**, *6* (6), 3267–3275. https://doi.org/10.1021/bm050313s.

(40)   Salam, A.; Venditti, R. A.; Pawlak, J. J.; El-Tahlawy, K. Crosslinked Hemicellulose Citrate-Chitosan Aerogel Foams. *Carbohydr. Polym.* **2011**, *84* (4), 1221–1229. https://doi.org/10.1016/j.carbpol.2011.01.008.

(41)   Ganesan, K.; Budtova, T.; Ratke, L.; Gurikov, P.; Baudron, V.; Preibisch, I.; Niemeyer, P.; Smirnova, I.; Milow, B. Review on the Production of Polysaccharide Aerogel Particles. *Materials (Basel).* **2018**, *11* (11), 1–37. https://doi.org/10.3390/ma11112144.

(42)   Gavillon, R.; Budtova, T. Aerocellulose: New Highly Porous Cellulose Prepared from Cellulose−NaOH Aqueous Solutions. *Biomacromolecules* **2008**, *9* (1), 269–277. https://doi.org/10.1021/bm700972k.

(43)   Tkalec, G.; Knez, Ž.; Novak, Z. Formation of Polysaccharide Aerogels in Ethanol. *RSC Adv.* **2015**, *5* (94), 77362–77371. https://doi.org/10.1039/C5RA14140K.

(44)   Takeshita, S.; Sadeghpour, A.; Malfait, W. J.; Konishi, A.; Otake, K.; Yoda, S. Formation of Nanofibrous Structure in Biopolymer Aerogel during Supercritical CO 2 Processing: The Case of Chitosan Aerogel. *Biomacromolecules* **2019**, *20* (5), 2051–2057. https://doi.org/10.1021/acs.biomac.9b00246.

(45)   Takeshita, S.; Konishi, A.; Takebayashi, Y.; Yoda, S.; Otake, K. Aldehyde Approach to Hydrophobic Modification of Chitosan Aerogels. *Biomacromolecules* **2017**, *18* (7), 2172–2178. https://doi.org/10.1021/acs.biomac.7b00562.

(46)   Sailakshmi, G.; Mitra, T.; Chatterjee, S.; Gnanamani, A. Chemistry Behind the Elastic Nature of the Biomaterial Prepared Using Oxidized Form of Glutaraldehyde and Chitosan - an Approach At 2D and 3D Level Subtitle: Glutaric Acid Cross-Linked Chitosan Biopolymer. *Int. J. Life Sci. Med. Res.* **2013**, *3* (2), 64–75. https://doi.org/10.5963/LSMR0302004.

(47)   Baldino, L.; Concilio, S.; Cardea, S.; De Marco, I.; Reverchon, E. Complete Glutaraldehyde Elimination during Chitosan Hydrogel Drying by SC-CO2 Processing. *J. Supercrit. Fluids* **2015**, *103*, 70–76. https://doi.org/10.1016/j.supflu.2015.04.020.

(48)   Shang, J.; Liu, S.; Ma, X.; Lu, L.; Deng, Y. A New Route of CO2 Catalytic Activation: Syntheses of N-Substituted Carbamates from Dialkyl Carbonates and Polyureas. *royasl Soc. Chem.* **2012**, *14*, 2899–2906. https://doi.org/10.1039/c2gc36043h.

(49)   Carretti, E.; Dei, L.; Baglioni, P.; Weiss, R. G. Synthesis and Characterization of Gels from Polyallylamine and Carbon Dioxide as Gellant. *J. Am. Chem. Soc.* **2003**, *125* (8), 5121–5129. https://doi.org/10.1021/ja034399d.

(50)   Kenneth H. Markiewitz, Wilmington, D. US3763106A- Polymers Preapred by Reacting Urea with an Amino Alcohol or Diamine Followed by Methylolation with Formaldehyde. US3763106A,

1973.

(51) Arnold, H. W. U.S Patent 2,145,242 - Process of Making Aliphatic Polyureas. US2145242 A, 1939.

(52) Gabler, R.; Müller, H. Preparation of Linear Polyureas Utilizing a Cyclic Amide Solvent. US3185656A, 1965.

(53) Chenite, A.; Gori, S.; Shive, M.; Desrosiers, E.; Buschmann, M. D. Monolithic Gelation of Chitosan Solutions via Enzymatic Hydrolysis of Urea. *Carbohydr. Polym.* **2006**, *64* (3), 419–424. https://doi.org/10.1016/j.carbpol.2005.12.010.

(54) Krajewska, B. A Combined Temperature-PH Study of Urease Kinetics. Assigning PKavalues to Ionizable Groups of the Active Site Involved in the Catalytic Reaction. *J. Mol. Catal. B Enzym.* **2016**, *124*, 70–76. https://doi.org/10.1016/j.molcatb.2015.11.021.

(55) Ganesan, K.; Heyer, M.; Ratke, L.; Milow, B. Facile Preparation of Nanofibrillar Networks of "Ureido-Chitin" Containing Ureido and Amine as Chelating Functional Groups. *Chem. - A Eur. J.* **2018**, *24* (72), 19332–19340. https://doi.org/10.1002/chem.201804405.

(56) Barrett, E. P.; Joyner, L. G.; Halenda, P. P. *The Determination of Pore Volume and Area Distributions in Porous Substances. I. Computations from Nitrogen Isotherms*; 1951; Vol. 73. https://doi.org/10.1021/ja01145a126.

(57) Reichenauer, G. Structural Characterization of Aerogels. In *Aerogels Handbook*; Aegerter, M. A., Leventis, N., Koebel, M. M., Eds.; Springer New York: New York, NY, 2011; pp 449–498. https://doi.org/10.1007/978-1-4419-7589-8_21.

(58) Stahl, T.; Brunner, S.; Zimmermann, M.; Ghazi Wakili, K. Thermo-Hygric Properties of a Newly Developed Aerogel Based Insulation Rendering for Both Exterior and Interior Applications. *Energy Build.* **2012**, *44* (1), 114–117. https://doi.org/10.1016/j.enbuild.2011.09.041.

(59) Barzagli, F.; Mani, F.; Peruzzini, M. From Greenhouse Gas to Feedstock: Formation of Ammonium Carbamate from CO2 and NH3 in Organic Solvents and Its Catalytic Conversion into Urea under Mild Conditions. *Green Chem.* **2011**, *13* (5), 1267–1274. https://doi.org/10.1039/c0gc00674b.

(60) Alexandrova, A. N.; Jorgensen, W. L. Why Urea Eliminates Ammonia Rather than Hydrolyzes in Aqueous Solution. *J. Phys. Chem. B* **2007**, *111* (4), 720–730. https://doi.org/10.1021/jp066478s.

(61) Mani, F.; Peruzzini, M.; Stoppioni, P. CO 2 Absorption by Aqueous NH 3 Solutions: Speciation of Ammonium Carbamate, Bicarbonate and Carbonate by a 13 C NMR Study. *Green Chem.* **2006**, *8* (11), 995–1000. https://doi.org/10.1039/b602051h.

(62) Matsuzaki, Y.; Yamada, H.; Chowdhury, F. A.; Higashii, T.; Kazama, S.; Onoda, M. Ab Initio Study of CO2 Capture Mechanisms in Monoethanolamine Aqueous Solution: Reaction Pathways from Carbamate to Bicarbonate. *Energy Procedia* **2013**, *37*, 400–406. https://doi.org/10.1016/j.egypro.2013.05.124.

(63) Yamamoto, Y.; Hasegawa, J. Y.; Ito, Y. Kinetic Investigation on Carbamate Formation from the Reaction of Carbon Dioxide with Amino Acids in Homogeneous Aqueous Solution. *J. Phys. Org. Chem.* **2012**, *25* (3), 239–247. https://doi.org/10.1002/poc.1900.

(64) Wang, X.; Conway, W.; Fernandes, D.; Lawrance, G.; Burns, R.; Puxty, G.; Maeder, M. Kinetics of the Reversible Reaction of CO2(Aq) with Ammonia in Aqueous Solution. *J. Phys. Chem. A* **2011**, *115* (24), 6405–6412. https://doi.org/10.1021/jp108491a.

(65) Walker, J.; Hambly, F. J. LXXVII.—Transformation of Ammonium Cyanate into Urea. *J. Chem. Soc., Trans.* **1895**, *67* (746), 746–767. https://doi.org/10.1039/CT8956700746.

(66) Yim, S. D.; Kim, S. J.; Baik, J. H.; Nam, I.; Mok, Y. S.; Lee, J.-H.; Cho, B. K.; Oh, S. H. Decomposition of Urea into NH 3 for the SCR Process . *Ind. Eng. Chem. Res.* **2004**, *43* (16), 4856–4863. https://doi.org/10.1021/ie034052j.

(67) Einbu, A.; Vårum, K. M. Depolymerization and De-N-Acetylation of Chitin Oligomers in Hydrochloric Acid. *Biomacromolecules* **2007**, *8* (1), 309–314. https://doi.org/10.1021/bm0608535.

(68) Kasaai, M. R.; Arul, J.; Charlet, G. Fragmentation of Chitosan by Acids. *Sci. World J.* **2013**, *2013*. https://doi.org/10.1155/2013/508540.

(69) Marji, T. J. Separation and Purification of Hydrophilic Polymers, M.Sc. in Pharmaceutical Technology 263467894, Jordan University of Science and Technology, 2008.

(70) Mattia, J.; Painter, P. A Comparison of Hydrogen Bonding and Order in a Polyurethane and Poly(Urethane-Urea) and Their Blends with Poly(Ethylene Glycol). *Macromolecules* **2007**, *40* (5), 1546–1554. https://doi.org/10.1021/ma0626362.

(71) Russo, P. S. A Perspective on Reversible Gels and Related Systems; 1987; pp 1–21. https://doi.org/10.1021/bk-1987-0350.ch001.

(72) Gurikov, P.; S.P., R.; Griffin, J. S.; Steiner III, S. A.; Smirnova, I. Solvent Exchange in the Processing of Biopolymer Aerogels: Current Status and Open Questions. *Ind. Eng. Chem. Res.* **2019**. https://doi.org/10.1021/acs.iecr.9b02967.

(73) Wong, J. C. H.; Kaymak, H.; Brunner, S.; Koebel, M. M. Mechanical Properties of Monolithic Silica Aerogels Made from Polyethoxydisiloxanes. *Microporous Mesoporous Mater.* **2014**, *183*, 23–29. https://doi.org/10.1016/j.micromeso.2013.08.029.

(74) Abdou, A.; Budaiwi, I. The Variation of Thermal Conductivity of Fibrous Insulation Materials under Different Levels of Moisture Content. *Constr. Build. Mater.* **2013**, *43*, 533–544. https://doi.org/10.1016/j.conbuildmat.2013.02.058.

(75) Zhao, S.; Malfait, W. J.; Demilecamps, A.; Zhang, Y.; Brunner, S.; Huber, L.; Tingaut, P.; Rigacci, A.; Budtova, T.; Koebel, M. M. Strong, Thermally Superinsulating Biopolymer-Silica Aerogel Hybrids by Cogelation of Silicic Acid with Pectin. *Angew. Chemie Int. Ed.* **2015**, *54* (48), 14282–14286. https://doi.org/10.1002/anie.201507328.

(76) Laufer, G.; Kirkland, C.; Cain, A. A.; Grunlan, J. C. Clay–Chitosan Nanobrick Walls: Completely Renewable Gas Barrier and Flame-Retardant Nanocoatings. *ACS Appl. Mater. Interfaces* **2012**, *4* (3), 1643–1649. https://doi.org/10.1021/am2017915.

(77) Leistner, M.; Abu-Odeh, A. A.; Rohmer, S. C.; Grunlan, J. C. Water-Based Chitosan/Melamine Polyphosphate Multilayer Nanocoating That Extinguishes Fire on Polyester-Cotton Fabric. *Carbohydr. Polym.* **2015**, *130*, 227–232. https://doi.org/10.1016/j.carbpol.2015.05.005.

(78) Bernhard, A. M. Catalytic Urea Decomposition, Side-Reactions and Urea Evaporation in the Selective Catalytic Reduction of NOx, ETH, 2012.

(79) Todorova, T.; Peitz, D.; Kröcher, O.; Wokaun, A.; Delley, B. Guanidinium Formate Decomposition on the (101) TiO2-Anatase Surface: Combined Minimum Energy Reaction Pathway Calculations and Temperature-Programmed Decomposition Experiments. *J. Phys. Chem. C* **2011**, *115* (4), 1195–1203. https://doi.org/10.1021/jp106523b.

(80) Pour, G.; Beauger, C.; Rigacci, A.; Budtova, T. Xerocellulose: Lightweight, Porous and Hydrophobic Cellulose Prepared via Ambient Drying. *J. Mater. Sci.* **2015**, *50* (13), 4526–4535. https://doi.org/10.1007/s10853-015-9002-4.

(81) Iswar, S.; Snellings, G. M. B. F.; Zhao, S.; Erni, R.; Bahk, Y. K.; Wang, J.; Lattuada, M.; Koebel, M. M.; Malfait, W. J. Reinforced and Superinsulating Silica Aerogel through in Situ Cross-Linking with Silane Terminated Prepolymers. *Acta Mater.* **2018**, *147*, 322–328. https://doi.org/10.1016/j.actamat.2018.01.031.

(82) Rudaz, C.; Courson, R.; Bonnet, L.; Calas-Etienne, S.; Sallée, H.; Budtova, T. Aeropectin: Fully Biomass-Based Mechanically Strong and Thermal Superinsulating Aerogel. *Biomacromolecules* **2014**, *15* (6), 2188–2195. https://doi.org/10.1021/bm500345u.

(83) Demilecamps, A.; Beauger, C.; Hildenbrand, C.; Rigacci, A.; Budtova, T. Cellulose–Silica Aerogels. *Carbohydr. Polym.* **2015**, *122*, 293–300. https://doi.org/10.1016/j.carbpol.2015.01.022.

(84) Cheng, Y.; Lu, L.; Zhang, W.; Shi, J.; Cao, Y. Reinforced Low Density Alginate-Based Aerogels: Preparation, Hydrophobic Modification and Characterization. *Carbohydr. Polym.* **2012**, *88* (3), 1093–1099. https://doi.org/10.1016/j.carbpol.2012.01.075.

(85)   Groult, S.; Budtova, T. Thermal Conductivity/Structure Correlations in Thermal Super-Insulating Pectin Aerogels. *Carbohydr. Polym.* **2018**, *196*, 73–81. https://doi.org/10.1016/j.carbpol.2018.05.026.

(86)   Plappert, S. F.; Nedelec, J.-M.; Rennhofer, H.; Lichtenegger, H. C.; Liebner, F. W. Strain Hardening and Pore Size Harmonization by Uniaxial Densification: A Facile Approach toward Superinsulating Aerogels from Nematic Nanofibrillated 2,3-Dicarboxyl Cellulose. *Chem. Mater.* **2017**, *29*, 6630–6641. https://doi.org/10.1021/acs.chemmater.7b00787.